Experimental and Numerical Study of Evaporation From Wavy Surfaces by Coupling Free Flow and Porous Media Flow

Bo Gao, Hossein Davarzani, Rainer Helmig, Kathleen Smits

AGU100 ADVANCING EARTH AND SPACE SCIENCE

Water Resources Research

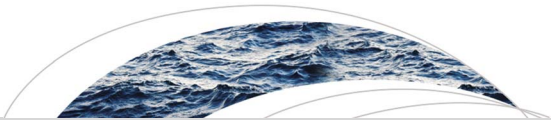

RESEARCH ARTICLE
10.1029/2018WR023423

Key Points:
- Evaporation involves fluid flow, vapor transport, and heat transfer between soil and atmosphere, described by coupling free flow and porous media flow model
- The macroscale surface roughness directly affects both atmospheric and diffusion-dominated stages I and II evaporation behavior, respectively
- The two main factors controlling the surface structure, surface waves, and aspect ratio have reverse effects on evaporations

Correspondence to:
B. Gao,
gaobo@mymail.mines.edu

Citation:
Gao, B., Davarzani, H., Helmig, R., & Smits, K. M. (2018). Experimental and numerical study of evaporation from wavy surfaces by coupling free flow and porous media flow. *Water Resources Research*, *54*, 9096–9117. https://doi.org/10.1029/2018WR023423

Received 4 JUN 2018
Accepted 23 OCT 2018
Accepted article online 30 OCT 2018
Published online 20 NOV 2018

Experimental and Numerical Study of Evaporation From Wavy Surfaces by Coupling Free Flow and Porous Media Flow

Bo Gao[1], Hossein Davarzani[2], Rainer Helmig[3], and Kathleen M. Smits[1,4]

[1]Department of Civil and Environmental Engineering, Colorado School of Mines, Golden, CO, USA, [2]Bureau de Recherches Géologiques et Minières, Direction Eau, Environnement et Ecotechnologies (D3E), Orléans, France, [3]Department of Hydromechanics and Modelling of Hydrosystems, University of Stuttgart, Stuttgart, Germany, [4]Department of Civil Engineering, University of Texas at Arlington, Arlington, TX, USA

Abstract The macroscale roughness of the soil surface has significant influences on the mass/energy interactions between the subsurface and the atmosphere during evaporation. However, most previous works only consider evaporation behavior from flat surfaces. Based on experimental and numerical approaches, the goal of this work is to provide a framework for the understanding of the mechanisms of evaporation from irregular soil surfaces at representative elementary volume scale. A coupling free flow-porous media flow model was developed to describe evaporation under nonisothermal conditions. For simplicity, sinusoidal-type wavy surfaces were considered. To validate this modeling approach, an experiment using an open-ended wind tunnel and soil tank was conducted. The experimental system was instrumented with various environmental sensors to continuously collect atmospheric and subsurface data. Results demonstrate that the surface roughness directly affects both atmospheric and diffusion-dominated stages I and II evaporation behavior, respectively. The atmospheric conditions directly affect the boundary layer during stage I. The evaporation rate is determined by the diffusion in the boundary layer, but not that in the porous media. The soil properties exert intrinsic influence on the capillary flow and determine the evaporation amount. The complex interaction between capillarity and the boundary layer leads to a heterogeneous distribution of evaporative flux with undulation (i.e., location along the soil surface) and time. Additionally, more and steeper waves indicate more influence from capillary flow, enhancing evaporation compared to a single wave system with the same wave amplitude, while steeper waves also result in a thicker boundary layer and weaken evaporation.

1. Introduction

Evaporation from bare soil surfaces is a key component of the global water cycle, which is closely tied to many industrial activities, climate modeling, weather prediction, agricultural crop growth modeling, and flood forecasting. In arid or semiarid settings, evaporation directly from soil can account for more than half of the total evapotranspiration and therefore critical to its understanding (Huxman et al., 2005). Even though decades of research have improved our understanding of evaporation at the laboratory and regional scales (Brutsaert, 1982; Budagovskij, 1964; Merta et al., 2006; Morton, 1983; Shao et al., 2018; Shuttleworth, 2007; Swenson & Lawrence, 2014), many knowledge gaps still exist in the current science on how the shallow subsurface interacts with the atmosphere during evaporation. Comprehensive understanding of the mechanisms involved in the atmosphere-subsurface interaction is significant to some relevant studies, such as the greenhouse gases emission (Pourbakhtiar et al., 2017) and the remediation of contaminated shallow soil (Weaver & Tillman, 2005). It is also helpful for further modification and improvement of the conventional general circulation models.

To date there have been many experimental and theoretical studies on flat-surface evaporation at different scales. Most previous experimental studies were conducted at the regional scale using different methods, such as eddy covariance, Bowen-Ratio energy balance, lysimeters, and water isotopes (e.g., Kool et al., 2014; Kustas & Agam, 2014). In terms of theoretical studies, the Community Land Model is one of the most frequently used models to simulate the fluid distribution within the whole ecological system (e.g., Oleson et al., 2010). But because of their complexity, these large, global, and regional-scale models/studies are oftentimes aimed at understanding the Earth's climate states or human behavior rather than investigating specific processes, like evaporation. This approach focuses on the entire evaporation amount while oversimplifing

the evaporation processes. Another theoretical approach is to use the Penman-Monteith equation alone to calculate evaporation in large-scale hydrological model on the precondition that all the parameters are known (Shao et al., 2018). Other experimental and modeling contributions at smaller scales include those by Lehmann et al. (2008), Shahraeeni et al. (2012), and Haghighi et al. (2013). Based on capillary bundle analysis, Lehmann et al. (2008) proposed a concept called characteristic lengths to define the evaporation stages at the representative elementary volume (REV) scale. REV is defined as the minimum volume of a porous medium sample in which a given geometrical property is independent of the size of the sample (Bear, 2013). It is the fundamental concept of continuum. Shahraeeni et al. (2012) developed a pore-scale model linking the surface water content with the inner capillary flow and the outer boundary layer for simulating evaporation. At the REV scale, Haghighi et al. (2013) employed the advection-diffusion equation in the laminar boundary layer to develop a generalized top boundary condition according to Ohm's law for evaporation, which uses the aerodynamic and soil resistance terms to incorporate the exchange processes between the soil and the atmosphere. Also, Penman-type equations are oftentimes used as top boundary conditions (Tang & Riley, 2013).

In addition to the above mentioned approaches, some researchers use more complex models on the basis of REV assumption to describe evaporation from flat surfaces. It is widely accepted that evaporation is a multiphase mass, momentum, and energy exchange process between the soil and the atmosphere, which can be significantly affected by the properties of both the soil (e.g., porosity, permeability, heterogeneity, and thermal and hydraulic conductivity) and the atmosphere (e.g., turbulence, air flow velocity, relative humidity, and radiation). All of these processes are strongly coupled and influence the soil-atmosphere interaction dynamically (Davarzani et al., 2014). The strong coupling between processes leads to highly dynamic interactions between the porous media properties, transport processes, and boundary conditions, resulting in dynamic evaporative behaviors (Sakai et al., 2011). However, the strong coupling at the land-atmosphere interface is rarely considered in most current models or practical application due to numerical model complexity and oftentimes a lack of experimental data needed to verify modeling approaches. But the use of the most complete form of multiphase flow equations in a fully coupled model allows for the investigation of the dominant mechanisms without any preliminary assumptions about the terms that are made in the formulation.

The concept of coupling free flow and porous media flow has been applied in various fields, including proton exchange membrane fuel cells (Baber, 2014), medicine movement inside an organ, multiphase flow through fractured-vuggy reservoirs (Huang et al., 2016), and evaporation from soil (Davarzani et al., 2014; Mosthaf, 2014; Mosthaf et al., 2014). In all these applications, one of the biggest challenges is the coupled interactions between the free flow and porous media flow. In general, there are two main conceptual approaches to describe this coupling, the one-domain and two-domain approaches. The one-domain approach is a simplified method to connect the free-flow and porous-media regions by assuming that the two regions are continuous in all their physical properties. Thus, only one flow equation, that is, the Brinkman equation (Goyeau et al., 2003), is applied in the entire system. According to the detailed conditions of each domain (i.e., free flow and porous media flow), the Brinkman equation is reduced to either the Navier-Stokes equation (free flow) or Darcy equation (porous media). Therefore, no specific interfacial boundary condition is defined between these two regions. Instead, a transition zone is defined where all the parameters (e.g., permeability and porosity) are continuous. As a result, the choice of these parameters in the transition zone significantly influence the modeling results. Additionally, the Brinkman model has yet to be demonstrated valid for multiphase flow. An alternative method, the two-domain approach, reduces the continuous transition zone to one, no-thickness interface. The Navier-Stokes and Darcy equations are applied separately on either side of this interface. Hence, extra interfacial conditions are imposed. Compared with single-domain approach, this approach has better extensibility, which is able to be extended to multiphase flow. For single-phase flow, similar results can be obtained by these two approaches, while the latter one is more numerically costly. But when multiphases are involved, two-domain approach is physical and accurate. This two-domain approach has been successfully used in multiphase coupling free-flow and porous-media flow problems (Baber et al., 2012; Davarzani et al., 2014; Han et al., 2014; Mosthaf et al., 2011; Tezduyar et al., 2008; Vanderborght et al., 2017).

Mosthaf et al. (2011) discussed the concept of coupling single-phase/two-components free flow and two-phases/two-components porous media flow in detail. They assumed that the interfacial conditions

were developed under mechanical, thermal, and chemical equilibrium according to phenomenological explications. The Beavers-Joseph condition (Beavers & Joseph, 1967) was assumed to be valid in the tangential direction of the interface though the condition originated from parallel single-phase flow. Mosthaf et al. (2014) applied this model to simulate evaporation from a flat, bare soil surface. Fetzer (2012) and Fetzer et al. (2016) extended this model by considering turbulent air flow over flat soil surfaces varying with sand grain roughness. They showed that the effects of the sand grain roughness were only visible for high velocities or large grain sizes. Compared with the above mentioned methods like energy balance, advection-diffusion equation, and generalized top boundary condition, the coupling free flow and porous media flow model is more complete and physically based. It allows us to improve our understanding of the heat, mass, and momentum transfer processes between the subsurface and the atmosphere during evaporation and provides us guidance for the improvement of simplified parameterizations (e.g., soil and atmospheric resistance terms) by assessing the dominant processes at the interface clearly.

Compared with the studies conducted for flat surfaces, the interaction between the shallow subsurface and the atmosphere is rarely considered for wavy soil surfaces. In this work, the term *wavy surface* refers to uneven soil surface with macroscale roughness (Canovaro et al., 2007), which is different from the generally recognized surface roughness formed by soil particles. The macroscale roughness here is 1 to 2 orders of magnitude larger than the particle-scale roughness and has a periodicity. In the experiment and modeling of this study, the roughness elements are on tens of centimeters tillage scale, not a hill with big atmosphere in nature. However, the introduction of this macroscale roughness is especially important to agricultural practices (e.g., soil tillage) though this study is only a simple lab-scale model. Tillage practices change the soil surface topology and soil properties, oftentimes resulting in an exposure of soil with high soil moisture content to the atmosphere and hence an increase in evaporation (the reverse can also occur; Unger & Cassel, 1991). Some factors such as tillage depth, surface relief, soil type, and evaporative demand can influence the drying characteristics of the tilled soils (Mwendera & Feyen, 1997). Therefore, the macroscale surface roughness is one of the important factors which should be taken into consideration. Several studies have shown that soil surface roughness affects water infiltration, water storage in surface depressions, and water runoff (Guzha, 2004; Lehrsch et al., 1987). Studies of energy transport across the soil surface show that the surface roughness can alter the reflectance of sunlight from cultivated soils and thus influence the surface energy balance (Matthias et al., 2000; Potter et al., 1987). Especially, in the case of turbulent atmospheric air flow, the mass and energy exchange process between the subsurface and the atmosphere are more complex for a wavy surface compared to a flat surface due to the formation of separation and reattachment areas, as well as different boundary layers (Baskaran et al., 1987; Buckles et al., 1984; Cherukat et al., 1998; Maaß & Schumann, 1996; Perry et al., 1969; Zilker & Hanratty, 1979). Taylor and Gent (1974) mentioned that the satisfactory inclusion of topography in atmospheric boundary layer models is a nontrivial problem. In other words, the macroscale surface roughness can affect each process associated with land-atmosphere interactions, including radiation, evaporation and drying, saturation distribution, and turbulence (Raupach & Finnigan, 1997). Despite the importance, few mechanistic studies have been conducted on evaporation from bare soil with macroscale roughness. The above mentioned studies that consider the relief of natural soil surfaces are either limited to field studies for agricultural purposes (Guzha, 2004; Lehrsch et al., 1987; Matthias et al., 2000; Mwendera & Feyen, 1997; Potter et al., 1987) or did not consider the physical processes within the porous media itself (i.e., within the soil; Maaß & Schumann, 1996; Cherukat et al., 1998; Kruse et al., 2006; Taylor & Gent, 1974; Wagner et al., 2011). Particularly, Haghighi and Or (2015) studied evaporation from wavy porous surfaces into turbulent free flow at the REV scale. In this study, they extended the expression of the aerodynamic resistance term that they developed for flat surfaces, in which the piecewise boundary layer thickness under turbulent air flow over wavy surfaces was taken into account. They conducted experiments using time domain reflectometry to qualitatively judge the contribution of valleys and ridges to evaporation based on the soil surface temperature distribution. Combined with a simple data analysis technique, the experimental temperature data were used to infer evaporation rates, which they then compared with predictions from the modified top boundary condition equation. This study showed that the mean evaporative flux across the wavy soil surface may be enhanced or suppressed compared with a similar flat surface. The authors inferred that the enhancement and suppression was due to the boundary layer thickness (thicker with wavy surfaces), the larger area present in wavy surfaces compared to flat surfaces and flux suppression in the separation flow

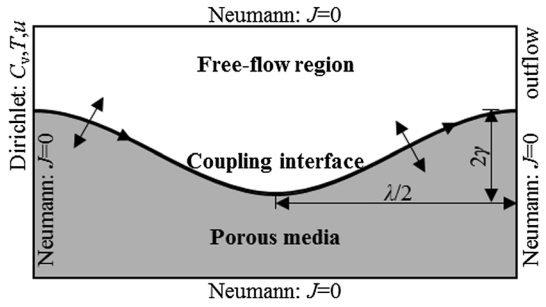

Figure 1. Two-dimensional configuration (subdomains and boundary conditions) where C_v is the water vapor concentration; T is temperature; u is wind speed; J is flux for T, u, and C_v; λ is wave length; and γ is half of the wave amplitude.

region. However, experimental and numerical results demonstrating this behavior were not presented as the simple models cannot describe all the physical processes in evaporation clearly.

The objectives of this study are to (i) develop a coupling free flow and porous media flow model to describe evaporation from wavy surfaces; (ii) perform a controlled bench-scale experiment to validate this model; (iii) improve our understanding of the characteristics of evaporation at the REV scale; (iv) investigate how and why the macroscale surface roughness influences the evaporation. For simplicity, to represent macroscale roughness (i.e., wavy surfaces) sinusoidal-type waves are considered. We emphasize that this study considers tens of centimeters roughness-surface model on lab scale. The results are based on the length scales of the experimental and numerical domains which may not truly mimic more realistic soil-atmosphere continuum scales at tens of thousands of meters due to heterogeneity.

According to the objectives, this paper is structured as follows: in section 2, we present the theoretical background and mathematical model to couple the flow and transport processes between the atmosphere and subsurface; in section 3, the experimental setup is described in detail; the numerical and experimental results are compared in section 4, first to validate the numerical model. Finally, the characteristics and influential factors of evaporation from wavy soil surfaces are discussed.

2. Mathematical Model

In this section, we present the mathematical description of heat and mass transfer of atmospheric air flow over uneven (i.e., wavy) permeable soil surfaces during evaporation. As introduced above, this process can be described by coupling free flow and porous media flow under nonisothermal conditions based on the REV-scale assumption.

This work is implemented on a two-dimensional configuration as shown in Figure 1. The width and the height of the whole system is 0.6 m and 0.3 m, respectively. For simplicity, the soil surface is represented by a simple sinusoidal line, which divides the system into two subdomains. The lower part is the shallow soil and the upper part is the free flow close to the soil surface. Wavy surfaces are usually characterized by aspect ratios, which is defined by $2\gamma/\lambda$ (where 2γ and λ are amplitude and wavelength, respectively). According to the two-domain approach, the equations in the atmosphere and the soil are defined separately, which are introduced here in detail.

2.1. Governing Equations for Free Flow

In the free flow, we assume that a single gas phase exists that is composed of two components, dry air and water vapor. The flow is nonisothermal and incompressible, and gravity is neglected. The fluid flow in the free-flow domain can be described by Navier-Stokes equation, assuming no thermal or solutal expansion (Bird et al., 2004):

$$\nabla\cdot\boldsymbol{u}_g^{ff} = 0 \tag{1}$$

$$\rho_g\frac{\partial\boldsymbol{u}_g^{ff}}{\partial t} + \rho_g\left(\boldsymbol{u}_g^{ff}\cdot\nabla\right)\boldsymbol{u}_g^{ff} = \nabla\cdot\left[-p_g^{ff}\boldsymbol{I} + \mu_g\left(\nabla\boldsymbol{u}_g^{ff} + \left(\nabla\boldsymbol{u}_g^{ff}\right)^{\mathrm{T}}\right)\right] \tag{2}$$

where the superscript "ff" denotes the free-flow region and the subscript "g" denotes the gas phase. $\boldsymbol{u}_g^{ff}$ (m/s) and p_g^{ff} (Pa) are the air flow velocity and pressure in the free-flow region; g (m/s^2) is the gravity acceleration; I is the unit matrix; ρ_g (kg/m^3) and μ_g (Pa·s) are the density and dynamic viscosity of the moist air, both of which depend on temperature and the fraction of water vapor in the gas. Their values are updated real time during calculation.

The component mass balance equation for water vapor in the free-flow region is defined by (Bird et al., 2004):

$$\frac{\partial\left(\rho_g w_v^{ff}\right)}{\partial t}+\nabla\cdot\left(\rho_g w_v^{ff}\boldsymbol{u}_g^{ff}\right)-\nabla\cdot\left[D_v^{ff}\nabla\left(\rho_g w_v^{ff}\right)\right]=0 \tag{3}$$

where w_v^{ff} is the mass fraction of water vapor in the gas phase and D_v^{ff} (m^2/s) is the diffusion coefficient in the free-flow region.

The energy balance equation in the free-flow region is (Kaviany, 2002):

$$\left(\rho_g c_{p,g}\right)\frac{\partial T^{ff}}{\partial t}+\left(\rho_g c_{p,g}\right)\nabla\cdot\left(\boldsymbol{u}_g^{ff}T^{ff}\right)-\nabla\cdot\left(\lambda_g\nabla T^{ff}\right)=0 \tag{4}$$

where T^{ff} is the temperature (K), $c_{p,g}$ (J/[kg·K]) is the heat capacity of the moisture air, and λ_g (W/[m·K]) is the thermal conductivity of gas mixture.

2.2. Governing Equations for Porous Media Flow

We assume that two phases, gas and water, exist in the porous media, and there are two components in the gas: water vapor and dry air. The dissolution of air in the water is neglected and these two fluids are immiscible. The two-phase flow in the porous media is always described by the generalized form of Darcy's law on the REV scale.

The mass balance equations of these two phases are (Bear, 2013):

$$\begin{aligned}\phi\frac{dS_w\partial(\rho_w p_c)}{dp_c\quad\partial t}+\nabla\cdot\left(\rho_w\boldsymbol{u}_w^{pm}\right)&=-f_{vw}\\ \phi\frac{dS_g\partial\left(\rho_g p_c\right)}{dp_c\quad\partial t}+\nabla\cdot\left(\rho_g\boldsymbol{u}_g^{pm}\right)&=f_{vw}\end{aligned} \tag{5}$$

where the superscript "pm" denotes the porous media and the subscript "w" denotes the water phase. S_i (i = w, g) is the saturation of i phase, ϕ is the porosity of the porous media, p_c is the capillary pressure between the water and gas, and f_{vw} is the water-gas phase change rate during evaporation, which will be explained in detail in Appendix A.

The velocity in equation (5) is determined by Darcy's law:

$$\begin{aligned}\boldsymbol{u}_w^{pm}&=-\frac{K_{int}k_{rw}}{\mu_w}\left(\nabla p_w^{pm}+\rho_w\boldsymbol{g}\right)\\ \boldsymbol{u}_g^{pm}&=-\frac{K_{int}k_{rg}}{\mu_g}\left(\nabla p_g^{pm}+\rho_g\boldsymbol{g}\right)\end{aligned} \tag{6}$$

where K_{int} is the intrinsic permeability of the soil; k_{ri} (i = w, g) is the relative permeability of i phase. The van Genuchten model is used for the water retention curve and relative permeability (van Genuchten, 1980); see Appendix A.

The mass balance equation for the two components in the gas is described by (Bear, 2013)

$$\phi\frac{\partial\left(\rho_g w_v^{pm}S_g\right)}{\partial t}+\nabla\cdot\left(\rho_g w_v^{pm}\boldsymbol{u}_g^{pm}\right)-\nabla\cdot\left[D_v^{pm}\nabla\left(\rho_g w_v^{pm}\right)\right]=f_{vw} \tag{7}$$

where D_v^{pm} is the effective diffusion coefficient in the porous media, which is determined by

$$D_v^{pm}=\phi S_g\tau D_v \tag{8}$$

where D_v is the gas phase diffusion coefficient (Campbell, 1985) and τ is the tortuosity of the porous media, which is estimated according to Millington and Quirk model (Millington & Quirk, 1961).

The governing equation for temperature in the porous media is given by (Whitaker, 1977):

$$\left(\rho c_p\right)_{\text{eff}}\frac{\partial T^{\text{pm}}}{\partial t}+\nabla\cdot\left[\left(\rho_{\text{g}}c_{p,\text{g}}\right)\boldsymbol{u}_{\text{g}}^{\text{pm}}T^{\text{pm}}+\left(\rho_{\text{w}}c_{p,\text{w}}\right)\boldsymbol{u}_{\text{w}}^{\text{pm}}T^{\text{pm}}\right]-\nabla\cdot\left(\lambda_{\text{eff}}\nabla T^{\text{pm}}\right)=-Lf_{\text{vw}}-Q_{\text{s}} \tag{9}$$

with

$$\left(\rho c_p\right)_{\text{eff}}=\phi S_{\text{w}}\rho_{\text{w}}c_{p,\text{w}}+\phi S_{\text{g}}\rho_{\text{g}}c_{p,\text{g}}+(1-\phi)\rho_{\text{s}}c_{p,\text{s}} \tag{10}$$

where $c_{\text{p},i}$ is the heat capacity of i phase (i = w, g, s) (J/[kg·K]); λ_i is the thermal conductivity of i phase (i = w, g, s) (J/[kg·K]); λ_{eff} is the effective thermal conductivity of all the phases including water, gas, and solid grain, which is defined by (Nield et al., 2006)

$$\lambda_{\text{eff}}=\phi S_{\text{w}}\lambda_{\text{w}}+\phi S_{\text{g}}\lambda_{\text{g}}+(1-\phi)\lambda_{\text{s}} \tag{11}$$

The subscript "s" in equations (10) and (11) denotes the solid phase. Q_{s} and L in equation (9) describe the energy losses from the soil tank and latent heat during water vaporization (Moradi et al., 2015).

2.3. Coupling Conditions on the Interface

Since different model concepts are used in the free flow and porous media regions, extra interfacial conditions are necessary to couple the two subdomains (Davarzani et al., 2014; Fetzer et al., 2016; Mosthaf & Baber et al., 2011) based on the assumption of local mechanical, chemical, and thermal equilibrium.

(1). Continuity of total mass flux
Considering there is only a gas phase that exchanges between the free-flow region and the porous media, the continuity of total mass flux in the normal direction of the interface should be

$$\left(\rho_{\text{g}}\boldsymbol{u}_{\text{g}}^{\text{ff}}\right)\cdot\boldsymbol{n}^{\text{ff}}=-\left(\rho_{\text{g}}\boldsymbol{u}_{\text{g}}^{\text{pm}}\right)\cdot\boldsymbol{n}^{\text{pm}} \tag{12}$$

where n denotes the normal vector of the interface.

(2). Continuity of normal stress
The normal stress at the interface is continuous:

$$\left\{\left[p_{\text{g}}^{\text{ff}}\boldsymbol{I}-\mu_{\text{g}}\left(\nabla\boldsymbol{u}_{\text{g}}^{\text{ff}}+\left(\nabla\boldsymbol{u}_{\text{g}}^{\text{ff}}\right)^{\text{T}}\right)+\rho_{\text{g}}\left(\boldsymbol{u}_{\text{g}}^{\text{ff}}\cdot\nabla\right)\boldsymbol{u}_{\text{g}}^{\text{ff}}\right]\boldsymbol{n}^{\text{ff}}\right\}\cdot\boldsymbol{n}^{\text{ff}}=p_{\text{g}}^{\text{pm}} \tag{13}$$

(3). Slip condition of tangential stress
In the tangential direction of the interface, the traditional Beavers-Joseph-Saffman (BJS) condition (Beavers & Joseph, 1967; Mosthaf, 2014; Mosthaf & Baber et al., 2011) is used to describe the tangential stress jump:

$$\left[\boldsymbol{u}_{\text{g}}^{\text{ff}}+\frac{\sqrt{K_{\text{int}}}}{\alpha_{\text{BJ}}}\left(\nabla\boldsymbol{u}_{\text{g}}^{\text{ff}}+\left(\nabla\boldsymbol{u}_{\text{g}}^{\text{ff}}\right)^{\text{T}}\right)\boldsymbol{n}^{\text{ff}}\right]\cdot\boldsymbol{t}_i^{\text{ff}}=0,\qquad i\in\{1,2,\ldots,d-1\} \tag{14}$$

where t^{ff} denotes the tangential vector at the interface, d is the dimension of the modeling system, and α_{BJ} is the slip coefficient. The value of the slip coefficient depends on the properties of the porous media and the fluids, as well as the grain size roughness of the interface, which is often empirically determined. According to Mosthaf (2014), Davarzani et al. (2014), and Huang et al. (2016), the slip coefficient has little influence on the model output. Thus, we set the slip coefficient to 0.01 for this study. In most studies, the BJS tangential condition is implemented under the condition that a single fluid phase exists throughout the whole system and the fluid flows parallel to the permeable porous media surface (Beavers & Joseph, 1967). However, because we assume laminar air flow velocity and the hypothesis that the two-phase water-gas at the top of the porous media has little influence on the tangential condition, we assume the BJS is still applicable in our model.

(4). Continuity of temperature and heat flux
Assuming local thermodynamic equilibrium, the temperature and the heat flux at the interface are continuous (Davarzani et al., 2014; Mosthaf, 2014; Mosthaf & Baber et al., 2011):

Table 1
List of Model Equations and the Primary Variables

Subdomain	Equation type	Equation number	Primary variables
Free-flow subdomain	Total mass continuity and Navier-Stokes	(1), (2)	$\boldsymbol{u}_g^{ff}, p_g^{ff}$
	Component mass balance for gas phase	(3)	w_v^{ff}
	Energy balance	(4)	T^{ff}
Porous-media subdomain	Total mass balance and Darcy's law	(5), (6)	p_w^{pm}, p_g^{pm}
	Component mass balance	(7)	w_v^{pm}
	Energy balance	(9)	T^{pmf}

$$T^{ff} = T^{pm} \tag{15}$$

$$\left[\left(\rho_g c_{p,g}\right)\boldsymbol{u}_g^{ff}T^{ff} - \lambda_g \nabla T^{ff}\right]\cdot\boldsymbol{n}^{ff} = -\left[\left(\rho_g c_{p,g}\right)\boldsymbol{u}_g^{pm}T^{pm} + \left(\rho_w c_{p,w}\right)\boldsymbol{u}_w^{pm}T^{pm} - \lambda_{eff}\nabla T^{pm}\right]\cdot\boldsymbol{n}^{pm} \tag{16}$$

(5). Continuity of vapor concentration and vapor flux is described by (Mosthaf, 2014; Mosthaf and Baber et al., 2011):

$$w_v^{ff} = w_v^{pm} \tag{17}$$

$$\left[\rho_g w_v^{ff}\boldsymbol{u}_g^{ff} - D_v^{ff}\nabla\left(\rho_g w_v^{ff}\right)\right]\cdot\boldsymbol{n}^{ff} = -\left[\rho_g w_v^{pm}\boldsymbol{u}_g^{pm} - D_v^{pm}\nabla\left(\rho_g w_v^{pm}\right)\right]\cdot\boldsymbol{n}^{pm} \tag{18}$$

A summary of the equations to be solved and their corresponding primary variables is listed in Table 1.

2.4. Boundary Conditions and Initial Conditions

As shown in Figure 1, the left, right, and bottom boundaries of the porous media are closed where Neumann conditions are applied:

$$-\boldsymbol{n}^{pm}\cdot\boldsymbol{u}_i^{pm} = 0, \qquad (i = w, g) \tag{19}$$

We assume that the center line of the free-flow region has the largest wind speed, which is considered as the top boundary, thus the following no viscous stress and normal flow conditions should be satisfied, where τ is the total viscous stress tensor:

$$\begin{aligned} &\boldsymbol{u}_g^{ff}\cdot\boldsymbol{n}^{ff} = 0 \\ &\boldsymbol{\tau} - \left(\boldsymbol{\tau}\cdot\boldsymbol{n}^{ff}\right)\boldsymbol{n}^{ff} = 0, \qquad \boldsymbol{\tau} = \left[\mu_g\left(\nabla\boldsymbol{u}_g^{ff} + \left(\nabla\boldsymbol{u}_g^{ff}\right)^T\right)\right]\boldsymbol{n}^{ff} \end{aligned} \tag{20}$$

The left boundary of the free-flow region is set as the inlet, where a laminar inflow with a constant average velocity, constant vapor concentration, and temperature are specifically defined. The right boundary of the free-flow region is the outlet and the manometer pressure is zero.

Initially, the porous media region is saturated with water. The vapor concentration in the free-flow region and the temperature of the whole system are the same as the inflow boundary. The mathematical model is implemented using COMSOL Multiphysics 5.2a (Comsol, 2016) based on the finite element method. The whole computation system was discretized with triangular mesh by 13,162 elements (71262DOFs). Local mesh refinement was applied at the interface due to possible formation of large gradients. An initialization was set up before the real calculation. The included linear parallel sparse direct solver (PARDISO) was used to implicitly solve the models.

3. Experimental Setup

To validate the above mathematical model, we designed an experimental system to simulate evaporation from a wavy soil surface. A series of data, including soil moisture, temperature, and pressure, as well as

Table 2
Important Porous Media Properties

Porosity	Bulk density	Saturated hydraulic conductivity	Intrinsic permeability	Residual water content	Thermal conductivity		Van Genuchten parameters (m = 1–1/n)	
ϕ	ρ_b[a]	K_{sat}[a]	K_{int}[a]	θ_r[a]	λ_{dry}[a]	λ_{sat}[a]	α[b]	n[b]
—	g/cm^3	m/s	m^2	—	W·m^{-1}·K^{-1}		m^{-1}	—
0.364	1.77	0.00036	3.5×10^{-11}	0.005	0.367	3.297	5	7

[a]Chamindu Deepagoda et al. (2016). [b]Forsythe (2017).

ambient relative humidity, temperature, and pressure are collected. This section presents the sand material properties, experimental apparatus and procedures in detail.

3.1. Sand Properties

A uniform silica sand, Accusand #50/70 (effective sieve number, Unimin Corp., Ottawa, MN) was used for this experiment. This sand has been widely characterized and used in previous works at the laboratory scale (Davarzani et al., 2014; Moradi et al., 2015; Sakaki & Illangasekare, 2007). Therefore, the key hydraulic/thermal properties are known (Table 2) and not used as fitting parameters so that the key physics can be more accurately described. This sand has low organic content and 99.8% quartz content, with a rounded grain shape. The uniformity coefficient, defined as d_{60}/d_{10}, is approximately 1.2 and the mean grain size d_{50} is 0.26 mm (Zhang et al., 2008). The porosity of the packed soil tank is about 0.364, similar to the experiments in (Forsythe, 2017; Zhang et al., 2008). The capillary pressure (P_c) and water content (θ_w) relationship was measured using a small Tempe cell apparatus (Forsythe, 2017). For convenience in numerical modeling, the van Genuchten model equation (A1) in section A1 was first used to fit the experimental $P_c - \theta_w$ data, and the fitting parameters α and n were obtained. Relevant properties of the porous media are listed in Table 2.

3.2. Development of Experimental Apparatus

A controlled bench-scale laboratory experiment was conducted using a low-velocity open-return wind tunnel that was interfaced with a 2-D soil tank as shown in Figure 2. The ductwork forming the wind tunnel is made of galvanized steel and oriented with the 2-D soil tank to channel air flow across the test section. To produce and control the wind, an in-line fan (Suncourt Pro Model DB6GTP) was connected to a velocity controller and a damper. The wind speed was continuously measured using a precalibrated pitot static tube (Dwyer Instruments, Inc.; Model 167–12; Accuracy ±5%) placed at the centerline of the tunnel. The soil tank was constructed with acrylic glass with length of 60 cm, height 30 cm, and width 9 cm. Compared with the length and width, the tank is thin and therefore can be considered as a two-dimensional tank.

As shown in Figure 2, 22 moisture sensors (Decagon Devices Inc., ECH$_2$O EC-5, moisture frequency 70 MHz, accuracy ±3%) were spaced at 10-cm increments horizontally and 5-cm increments vertically throughout the tank. Measurements were collected as analog to digital converter counts and then converted to soil moisture using the two-point α-mixing model (Sakaki et al., 2008). The subsurface temperature was monitored using 14 temperature sensors (Decagon Devices Inc., RT-1, accuracy ±0.5 °C for measurement from 5 to 40 °C). Eleven pressure sensors (Tensiometer, Soilmoisture Equipment Corp., Goleta, CA; pressure transducer, Omega Engineering, Inc., Stamford, CT, Model PX26 Series, accuracy ±1% psi for the range 0–250 psi, operating temperature: −40 to 85 °C) were located throughout the tank to measure the pore water pressure. The moisture, temperature, and pressure sensors were inserted horizontally through the sides of the acrylic

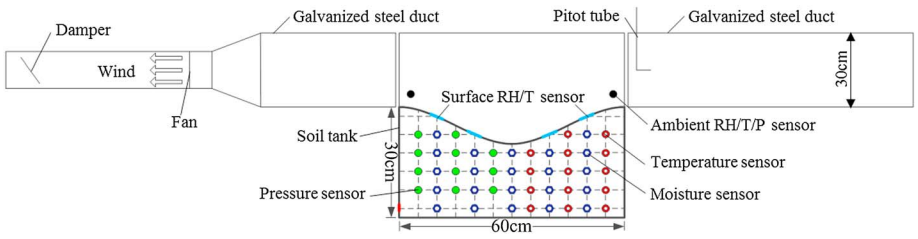

Figure 2. Schematic of the experimental system.

Table 3
Average Atmospheric Experimental Data

Time	Wind speed (m/s)	Temperature (K)	Vapor concentration (kg/m^3)	Pressure (kPa)
$t \leq 18$ days	0.08	293.8	0.0064	82.54
$t > 18$ days	0.08	296.3	0.0036	82.54

tank to minimize their volume within the tank and hence their effect on the flow processes within the tank. At the soil surface, there were four sensors distributed uniformly to record the surface relative humidity and temperature (Decagon Services, Inc., EHT RH/temperature, accuracy ±2% from 5 to 90% RH; ±3% from 90 to 100% RH; temperature accuracy ±0.25 °C). The relative humidity/temperature sensors were placed in contact with the soil grains directly. In addition four VP-4 sensors (Decagon Devices, Inc.; resolution 0.1% RH, 0.1 °C temperature, and 0.01 kPa pressure; accuracy ±5% RH, ± 0.5 °C temperature, ± 0.4 kPa pressure) were located above the soil surface (two at the inlet of the free-flow region, two at the outlet, see Figure 2) to measure the atmospheric relative humidity, temperature, and pressure. All the moisture, temperature, and relative humidity sensors were connected to Em50 series data loggers (Decagon Services, Inc., ECH$_2$O System) to store the corresponding data hourly.

3.3. Experimental Procedures

The subsurface moisture, temperature, and pressure sensors were tested and calibrated first and then inserted into the corresponding locations of the soil tank. The tank was then wet-packed with #50/70 silica sand (Accusand, Unimin Corporation, Ottawa, MN) in incremental 2-cm layers to achieve a uniform bulk density (Sakaki & Illangasekare, 2007). The soil surface was constructed using a prefabricated metal mold as a sinusoidal-type wavy shape with a wave amplitude of 5 cm, as shown in Figure 2. We did our best to make sure the water table was initially at the soil surface. However, because of the wavy shape, a small amount of water accumulated at the bottom of each wave (i.e., in the valley) which was unavoidable based on the soil properties. Before starting the experiment, the soil surface was covered with plastic wrap to prevent evaporation. The side and the bottom walls of the tank did not allow for fluid flow and the valve at the bottom of the tank was shut off so that no water was supplied at the bottom boundary. Then, the tank was placed on a scale (Sartorius Model 11209–95, Range 65 kg, Resolution ±1 g) to continuously monitor the water loss from the system. The wind tunnel fan was then set to a constant low speed of 0.08 m/s. A low wind speed was selected to maintain laminar flow conditions (Re ~ = 580), considering the design of the soil tank, the wind tunnel, and the measurement accuracy of the pitot tube. Thus, turbulence could be neglected. Finally, the plastic wrap was removed from the soil surface and the experiment was initiated; the experiment was run for 46 days.

4. Results and Analysis

In this section, the experimental and numerical results are first compared to validate our modeling approach. This is followed by a discussion of the evaporation behavior at the REV scale and an analysis of several factors such as atmospheric conditions, soil properties, and surface structure.

4.1. Comparison of Numerical and Experimental Results

Experimental and numerical results are first compared to verify the coupling model presented in section 2. Experimental data to include the wind speed and temperature in the air flow and the vapor concentration (determined based on the relative humidity) were used as the boundary conditions in the simulation (see Table 3). It is important to note that the laboratory central heating system was turned on at day 18 of the experiment. Therefore, the average ambient temperature increased by ~3 °Kelvin, according to the data. Thus, the simulation was divided into two sections due to the changes of boundary conditions (see Table 3). This change influenced the one fitting parameter of the model, b, in the phase change rate expression. For $t \leq 18$ days b was 1.2×10^{-4} s/m^2 and for 5.8×10^{-5} s/m^2 after 18 days by fitting the cumulative evaporation data. The corresponding equilibrium time $1/B$ (The definition of B is shown in section A2.) for phase change is on the order of magnitude 0 (10^{-1}), which is similar to other transport time scales (e.g., capillary diffusion and heat flow; Halder et al., 2011). It also indicates that nonequilibrium phase change should be taken into consideration.

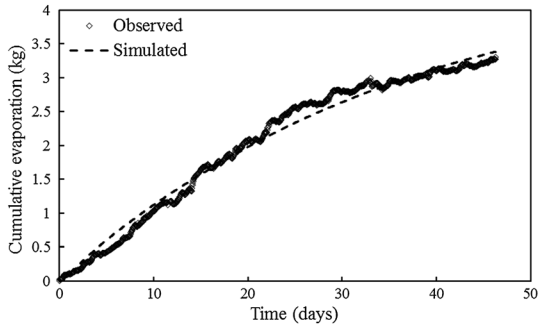

Figure 3. Comparison of the simulated and observed cumulative evaporation over time (rhombus marks = the observed data from experiment; dash line = the simulated results by modeling).

Figure 3 shows the comparison of the simulated and observed cumulative evaporated mass over time. Generally, there is a good agreement between the simulated and experimental results with a R^2 value of 0.987. The observed soil evaporation curve shows relatively gentle changes with time and does not present obvious drying stages owing to the very low wind speed (0.08 m/s) in this experiment. The evaporation remained in stage I for about 30 days and came to stage II without an obvious transition period.

Figure 4a shows the time distribution of soil moisture for four measurement depths (7.5, 12.5, 17.5, and 22.5 cm below the soil surface). The numerical model could predict the evolution of the soil moisture well at the early times but failed to capture the moisture at later times (i.e., ~ t = 20 days). The R^2 values for the depths 7.5, 12.5, 17.5, and 22.5 cm are 0.93, 0.92, 0.92, and 0.92, respectively. Figure 4b compares the observed and simulated moisture profiles at x = 10 cm (the first moisture sensor column) at three different times (10, 20, and 35 days). The R^2 values for this comparison are 0.99, 0.98, and 0.97 at times t = 10, t = 20, and t = 35 days, respectively. Figure 4b also indicates that the model cannot give a good prediction of the soil moisture evolution after 20 days. This could be due to, in part, the change in the bulk density of the soil with depth that is oftentimes seen in both experiments and field conditions (Assouline, 2006). In addition, the accuracy of the soil moisture sensors and the local heterogeneity formed during soil packing as discussed in section 3 could also contribute to this difference. Another consideration is the definition of some of the fluid properties in the numerical simulations (e.g., density, viscosity, and diffusion coefficient). All these properties are empirically derived, which could lead to compounding inaccuracies in modeling results. However, the numerical model performs relatively well.

Figure 5 displays the distribution and location of the moisture sensors used in the experiment. We selected seven locations labeled as #1, #2, #6, #10, #14, #18, and #19 to investigate the soil moisture dynamics below the wavy surface with time. The horizontal coordinates of the seven points are x = 10, 10, 20, 30, 40, 50, and 50 cm, respectively. The sensors #2, #6, #10, #14, and #19 are located along the same horizontal plane. The sensor locations #1, #6, #14, and #18 are 5 cm below the wavy surface; #2 and #19 are 10 cm below the surface; and #10 is 2.5 cm below the surface.

Figure 6a shows the evolution of soil moisture with time (from 0 to 25 days) at four points (#1, #6, #14, and #18), which are 5 cm below the wavy surface. The experimental curves from the left to the right in Figure 6a corresponds to the measurement locations #18, #1, #14, and #6. Relatively, sensors #14 and #18 are located closer to the air intake compared with #6 and #1. The air flows from right to left. The wind slows down when it flows downward and accelerates when it climbs up. Thus, the viscous boundary layer has the largest thickness at the valley and the boundary layer thickness should be symmetrical to the vertical center axis of the soil tank. However, we consider that the vapor is carried from right to the left and accumulates more at the left. The vapor concentration gradient should be smaller at the uphill. That is why we see that #18 evaporates faster than #1 and #14, faster than #6. The four points are all located 5 cm below the

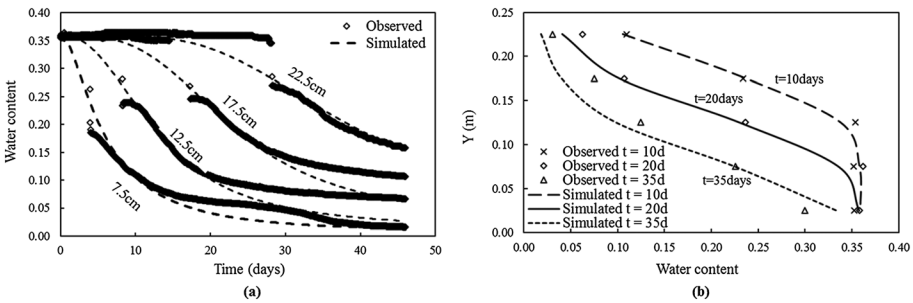

Figure 4. (a) Comparison of subsurface moisture evolution with time (rhombus marks in a = the observed data from experiment; dash line = simulated results by modeling) and (b) moisture profile at x = 10 cm.

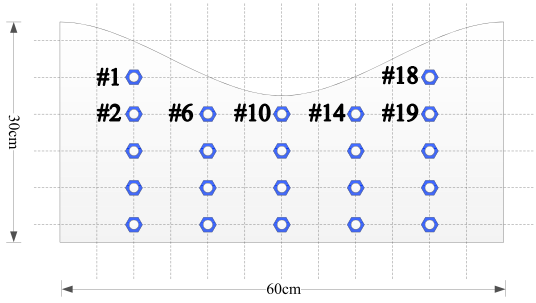

Figure 5. Schematic of the distribution and location of the moisture sensors.

surface. But the water at #1 and #18 evaporates first, although #1 is farther from the fan compared with #14. One may notice that the moisture recorded by sensor #18 has a quick decrease and then an increase during the half day of the beginning. This may be due to the local heterogeneous distribution of water, water supply from the surrounding soil, and/or measurement error, since this phenomenon is only seen at location #18.

Figure 6b shows the evolution of soil moisture with time (from 0 to 20 days) at points #2 and #10. Sensor #2 is located below the upper downslope surface and #10 is just below the valley, while they are at the same horizontal line. Clearly, evaporation first happens at #2 although #10 is much close to the surface. Figure 7 shows the moisture distribution along one horizontal line where the sensors #2, #6, #10, #14, and #19 are located at 1, 10, and 11 days. Obviously, the soil loses water at the peaks first (from the two sides to the middle). But the moisture distribution and the evolution of the distribution are not symmetric to $x = 30$ cm as explained above. Therefore, Figures 6 and 7 demonstrate that evaporation from a wavy surface is not the same along the surface and the peaks evaporate prior to the valleys. Detailed analyses are presented in the later simulated results.

4.2. Typical Evaporation Rate Curve

Figure 8 shows the simulated evaporation rate (solid line) and diffusive flux (dashed line) over time. Although not shown, the observed evaporation rate showed similar behavior (see section 4.1 for experimental results). The evaporation rate in Figure 8 was calculated according to the loss of water in the porous media subdomain (see Figure 1) by

$$\mathrm{Loss}_{\mathrm{w,pm}} = \rho_{\mathrm{w}}\left(\phi - \theta_{\mathrm{g}}\right)V_{\mathrm{pm}} \tag{21}$$

where V_{pm} is the volume of the porous media subdomain.

The dashed line in Figure 8 was calculated based on Fick's law along the soil surface

$$E = \int D\nabla\left(\rho_{\mathrm{g}} w_{\mathrm{v}}\right)\,\mathrm{d}l \tag{22}$$

where D is the diffusion coefficient, which equals $D_{\mathrm{v}}^{\mathrm{pm}}$ in the porous media and $D_{\mathrm{v}}^{\mathrm{ff}}$ in the free-flow region, w_{v} is the fraction of vapor in gas, and l denotes the length of the soil surface.

The porous media diffusion coefficient $D_{\mathrm{v}}^{\mathrm{pm}}$ was used here to obtain the dashed line in Figure 8, representing the amount of water vapor generated in the porous media that leaves the soil via diffusion per day. The amount of vapor loss across the surface due to advection was ignored here due to the assumption of very slow laminar flow.

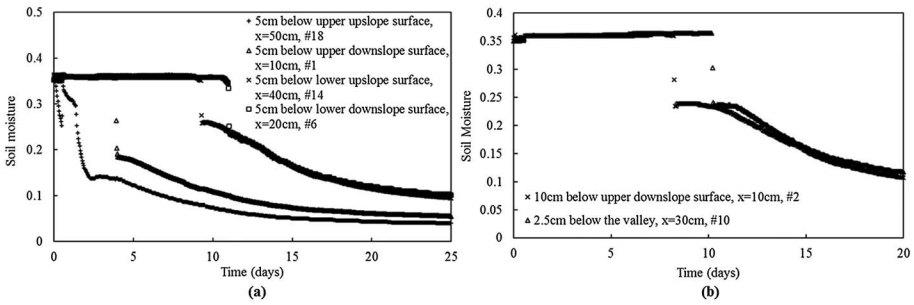

Figure 6. (a) Evolution of soil moisture with time in the experiment at four points located 5 cm below the wavy surface. The corresponding marks of these four points are #1, #6, #14, and #18 shown in Figure 5. The horizontal location of these four points are $x = 10$, 20, 40, and 50 cm, respectively. (b) Evolution of soil moisture with time at two points, #2 and #10 (Figure 5), which are located along the same horizontal line. The horizontal location of these two points are $x = 10$ and 30 cm, respectively. Points #2 and #10 are 10 and 2.5 cm below the wavy surface, respectively.

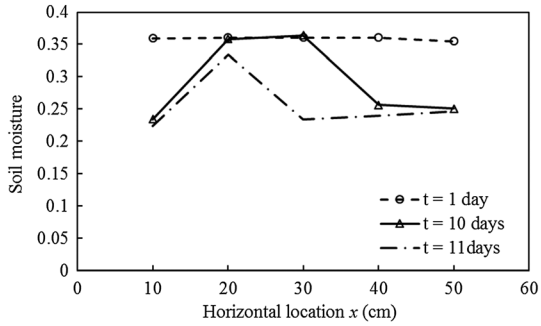

Figure 7. The experimental moisture distribution along one horizontal line where the sensors #2, #6, #10, #14, and #19 are located at t = 1, 10, and 11 days. The horizontal location of these five sensors are x = 10, 20, 30, 40, and 50 cm, respectively. Sensors #2 and #19 are 10 cm below the wavy surface; sensors #6 and #14 are 5 cm below the wavy surface; and sensor #10 is 2.5 cm below the wavy surface.

The shape of the evaporation rate curve is controlled by two factors. One is the continuous capillary water flow, which can provide liquid water to the vaporization plane where it changes phase and evaporates. The other is vapor diffusion inside the soil. During stage I, the vaporization plane is at the soil surface as there is continuous water replenishing the soil surface due to capillary flow. However, the top part of the porous media gradually becomes unsaturated. Water vapor moves via diffusion through this unsaturated zone and leaves the porous media across the boundary layer to the atmosphere. During stage I, the effect of water flow due to capillarity (capillary flow) is much more important than vapor diffusion in the porous media and the evaporation rate is relatively constant or decreases slowly. As less and less water reaches the soil surface, the influence of vapor diffusion in the porous media increases gradually. As the influence of diffusion increases, the evaporation rate decreases sharply; this is usually referred to as the transition between stages I and II. However, even though the importance of diffusion increases, during this transition, the capillary flow still dominates. Theoretically speaking, if we just use Fick's law in this unsaturated zone to calculate the evaporation, we will underestimate the evaporation rate since continuous capillary flow still plays an important role in this zone (see stage I and transition in Figure 8). Therefore, for stage I, the evaporation rate can accurately be determined by calculating the water mass loss in the porous media subdomain (equation (21)) and the solid line in Figure 8. Differently, the vapor moves across the boundary layer only by diffusion. Thus, Fick's law can be used for the estimation of evaporation rate during stage I and the transition stage within the boundary layer only (i.e., not in the porous media).

When evaporation enters stage II, the continuous water flow can no longer reach the soil surface and a dry zone forms near the soil surface. At the same time, the vaporization plane continues to recede into the porous media (i.e., moves down). The continuous water arrives at this receding vaporization plane and changes to vapor. The vapor moves across both the dry zone of the porous media and the boundary layer totally by diffusion. That is to say, the evaporation rate obtained by Fick's law in the dry zone equals that in the boundary layer; and both of them are equal to the value calculated by water mass loss in the porous media subdomain (see stage II and the solid line in Figure 8). Thus, we can locate the exact time of the onset of stage II, which is the time when Fick's law is valid in the porous media to calculate the evaporation rate. Here we discussed the relationship of the two methods, the loss of water and Fick's law, to calculate the evaporation rate at the REV scale (Figure 8). Interested readers can refer to Lehmann et al. (2008) for a similar discussion but based on pore-scale understanding. Based on these theories, nearly all the different shape evaporation rate curves influenced by various factors can be explained and understood.

Davarzani et al. (2014) simulated cumulative evaporation under different wind speeds, atmospheric vapor concentrations, permeability, etc. for a flat soil surface. Mosthaf et al. (2014) also studied the influence of permeability, van Genuchten parameters, etc. on the evaporation rate behavior for flat surfaces. They concluded that larger wind speeds and lower vapor concentrations result in higher evaporation rates in stage I and a shorter transition to stage II; changing permeability does not change the evaporation in stage I significantly but increasing permeability increases the transition; a lower van Genuchten parameter n leads to a prolonged stage 1. However, they did not explain the characteristics and mechanisms of the evaporation curves for different factors during both stages of evaporation. Because both cumulative evaporation and evaporation rate are comprehensive concepts based on the REV assumption, some local characteristics and the value of cumulative evaporation as well as evaporation rate may be distinct for different surface configurations. But compared with a flat surface, similar influences of the atmospheric conditions and soil properties on the evaporation rate (or cumulative evaporation) can be seen in the case of wavy surfaces. Therefore, in the following two sections, only some representative factors are discussed in order to provide the reader a clearer

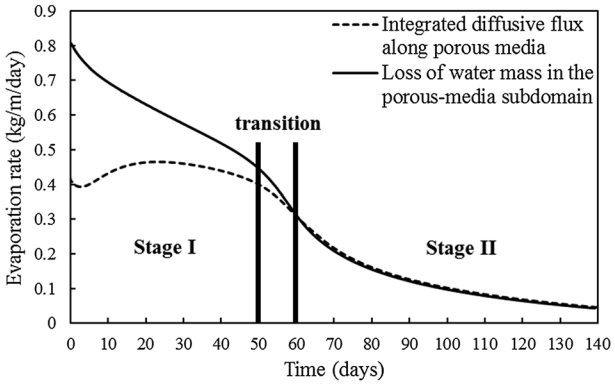

Figure 8. Typical evaporation rate curve by coupling model.

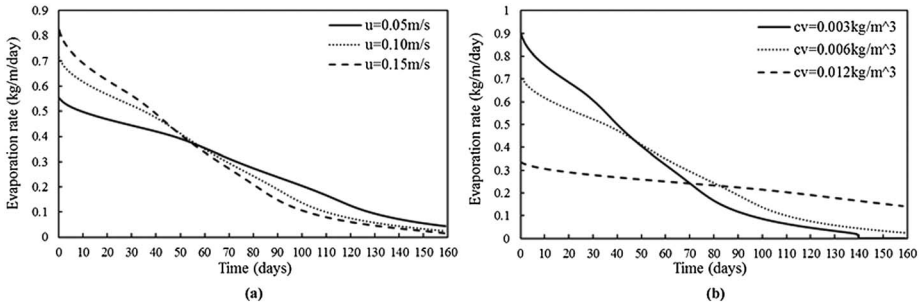

Figure 9. (a) Impact of air flow velocity (wind speed) on evaporation rate ($C_{v,inlet}$ = 0.006 kg/m^3, T_{inlet} = 293.15 K, K = 1E−10 m^2, ϕ = 0.312, α = 8, n = 5, AR = 1/6). (b) Effect of ambient vapor concentration on evaporation rate ($u_{g,inlet}$ = 0.10 m/s, T_{inlet} = 293.15 K, K = 1E−10 m^2, ϕ = 0.312, α = 8, n = 5, AR = 1/6).

understanding of how and why these factors respond during the entire evaporation process. The particular differences due to the surface configuration will be analyzed in detail in section 4.5. The analyses in the following three sections are all based on numerical modeling results.

4.3. Effects of Atmospheric Conditions

Atmospheric conditions to include wind speed, relative humidity, and temperature provide the necessary external conditions for the entire evaporation system. Conceivably, they may affect evaporation directly through changing the characteristics of the boundary layer, which connects the atmosphere and the soil.

Figure 9a shows the evaporation rate under different ambient air flow wind speeds of 0.05, 0.10, and 0.15 m/s; Figure 9b shows the evaporation rate under different ambient vapor concentrations of 0.003, 0.006, and 0.012 kg/m^3. The vapor concentrations were selected based on the corresponding ambient relative humidity of 17.4%, 34.7%, and 69.4% under 20 °C.

From the discussion in section 4.2, we know that the capillary flow provides water to the surface and dominates during stage I; the evaporation rate is decided by the vapor diffusion in the boundary layer. The boundary layer for a flat surface can be defined as a function of wind speed according to the definition

$$\delta_m = 5\sqrt{\frac{\mu_g x}{\rho_g U_\infty}} \tag{23}$$

where U_∞ is the average atmospheric wind speed in the free-flow region and x is the abscissa value. As the wind speed decreases, the thickness of the boundary layer for a flat surface increases. This trend is assumed to be the same in the case of wavy surfaces. Under low wind speeds, the application of Fick's law inside the boundary layer will result in a lower evaporation rate than at high wind speeds. In addition, the water content near the soil surface and the vapor concentration gradient within the boundary layer will change slowly. Thus, stage I will be relatively long, as shown in Figure 9. Figure 10 depicts the distribution of the surface water saturation at t = 1 day. Different from the water saturation along the flat surface, the water evaporates first at the ridges. The increasing wind speed requires higher demand of evaporation, which also results in lower soil surface moisture. Combined with the consideration of the thinner boundary layer, one can infer that the local diffusive flux at the ridges should be larger than that of the valley at least at the beginning of the evaporation. It will be discussed in detail in the later section.

Similarly, under low ambient vapor concentrations (e.g., C_v = 0.003 kg/m^3), the difference of vapor concentration between the porous media and the free flow is large, and the corresponding gradient within the boundary layer is high. Thus, during stage I when the evaporation rate is decided by the vapor diffusion in the boundary layer, the evaporation rate will be higher for a lower ambient vapor concentration. However, both wind speed and ambient vapor concentration are external influential factors which have no impact on the total evaporative mass over time. Higher evaporation rates at the early stage then result in smaller evaporation rates at later stages. Thus, one can see that the curves in both Figures 9a and 9b cross at some day and finally converge to zero.

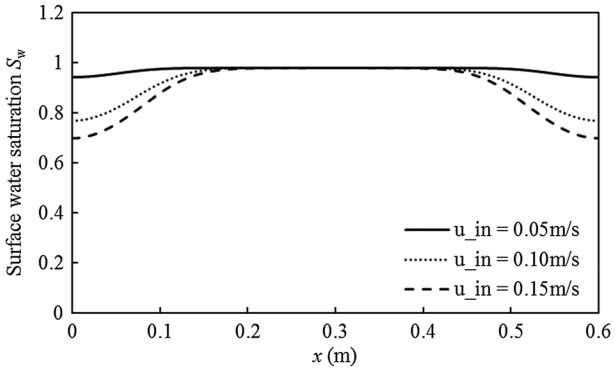

Figure 10. Water saturation distribution at the surface during stage I (t = 1 day) under different air flow velocities ($C_{v,inlet}$ = 0.006 kg/m^3, T_{inlet} = 293.15 K, K = 1E−10 m^2, ϕ = 0.312, α = 8, n = 5, AR = 1/6).

In summary, the ambient conditions (e.g., wind speed and vapor concentration) affect the behavior of the boundary layer directly, which further affect the evaporation rate during stage I when vapor diffusion occurs in the boundary layer but not the long-term evaporative mass over time. This also demonstrates our conjecture mentioned above.

4.4. Effects of Soil Properties

Phase change from liquid water to water vapor occurs at the vaporization plane within the porous media. The soil properties, like permeability, porosity, and soil-water retention, are the internal or intrinsic conditions controlling the evaporation. They affect evaporation by influencing the capillary flow and thus influencing the vapor concentration at the soil surface. In this section, we show the influence of the intrinsic permeability and the van Genuchten parameter n, as examples of the effects of soil properties on evaporation.

Figure 11a presents the evaporation rate for different permeability porous media, assuming other properties of the porous media remain constant. The basic theory is still that the capillary flow dominates during stage I and the evaporation rate is decided by the vapor diffusion in the boundary layer. At early stage I, since the surface moisture is high and the vapor concentration gradient inside the boundary layer is relatively stable, permeability has little influence. Permeability is an intrinsic property of the porous media, representing the ability of fluid to flow though the porous media; high permeability correlates with higher capillary flow and hence more water moving to the vaporization plane with time. Therefore, media with a high permeability will have longer stage I evaporation. For low-permeability media, the unsaturated or dry zone will emerge early, resulting in the early appearance of stage II. Since the ability of the capillary flow may vanish early in the large-permeability porous media, its influence, though also small, lasts relatively long in the low-permeability porous media. Therefore, from Figure 11a we can see that at late stage II, the evaporation rate of the porous media with higher permeability may be slightly lower.

Figure 11b demonstrates the influence of the van Genuchten parameter, n on the evaporation rate. This parameter affects both the air entry value (a large n correlates to a high air entry value) and the shape of the soil-water retention curve, especially during water drainage. Again, capillary flow dominates during stage I, and the evaporation rate is decided by the vapor diffusion in the boundary layer. First, for a soil with a high n value, more effort is needed for the atmospheric air to overcome the soil resistances, mainly those from water gravity and hence enter the porous media and displace the water at the vaporization plane. In other words, it is relatively difficult to keep the surface water content at a high value by capillary flow after the surface water evaporates. Thus, the high n value lowers both the vapor concentration at the surface and the vapor concentration gradient in the boundary layer, leading to a lower evaporation rate than that for a small n value. After air eventually enters the porous media, water drainage is easier for large-n material. Capillary flow plays a more important role but will not last long, increasing the evaporation process and resulting in a shorter stage I and faster transition to stage II.

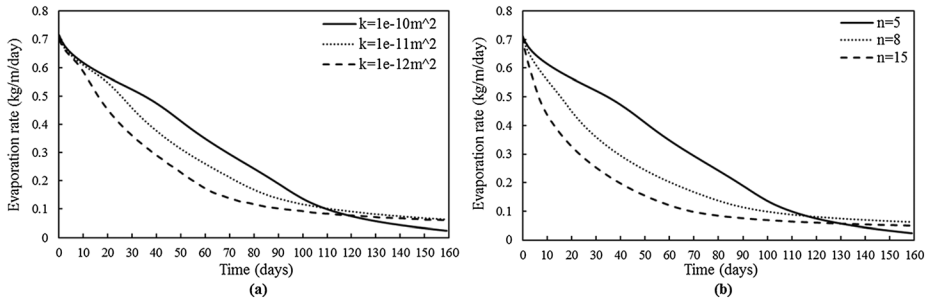

Figure 11. (a) Effect of intrinsic permeability on evaporation rate ($u_{g,inlet}$ = 0.10 m/s, $C_{v,inlet}$ = 0.006 kg/m^3, T_{inlet} = 293.15 K, ϕ = 0.312, α = 8, n = 5, AR = 1/6). (b) Effect of van Genuchten parameter n on evaporation rate ($u_{g,inlet}$ = 0.10 m/s, $C_{v,inlet}$ = 0.006 kg/m^3, T_{inlet} = 293.15 K, K = 1E−10 m^2, ϕ = 0.312, α = 8, AR = 1/6).

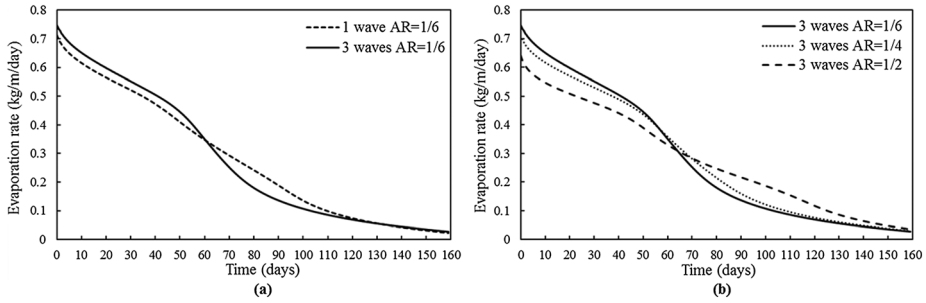

Figure 12. (a) Effect of wave numbers on evaporation rate ($u_{g,inlet}$ = 0.10 m/s, $C_{v,inlet}$ = 0.006 kg/m^3, T_{inlet} = 293.15 K, K = 1E−10 m^2, ϕ = 0.312, α = 8, n = 5). (b) Effect of aspect ratio (AR) on evaporation rate ($u_{g,inlet}$ = 0.10 m/s, $C_{v,inlet}$ = 0.006 kg/m^3, T_{inlet} = 293.15 K, K = 1E−10 m^2, ϕ = 0.312, α = 8, n = 5, 3 waves).

Unlike the atmospheric conditions which affect the boundary layer directly, the soil properties have a direct influence on the continuous capillary flow. The capillary flow determines the volume of water moving to the vaporization plane and how much vapor exists at the surface, which is related with the vapor concentration gradient (vapor diffusion) in the boundary layer.

4.5. Effects of Macroscale Roughness

The effects of atmospheric conditions and soil properties on the evaporation from wavy surfaces are discussed in the last two sections. The author also ran simulations to test their effects in the case of flat surface and found that the curves present similar trend but not the same value due to the macroscale roughness. This section focuses on the wavy surfaces and make clear the influences and the corresponding mechanisms.

The two main factors that may affect the macroscale roughness are the number of surface waves and their aspect ratio. The former denotes the soil surface undulations, while the latter represents the undulation steepness. The aspect ratio is defined by (Haghighi & Or, 2015)

$$AR = 2\gamma/\lambda \tag{24}$$

where γ and λ are the amplitude and length of the wavy surface, respectively.

The comparison of evaporation rate under different aspect ratios and number of surface waves is shown in Figures 12a and 12b, respectively. Both increasing the number of surface waves and aspect ratio will increase the area of the vaporization plane in stage I, which provides better opportunity for the contribution of capillary flow. In the case of more waves (Figure 11), the evaporation rate is larger and sustained longer in stage I. However, as previously mentioned, since the total amount of water for evaporation is determined by the intrinsic properties of the porous media, a higher evaporation rate in stage I results in a lower evaporation rate in stage II. Capillary flow contributes more to stage I evaporation when there are more waves, leading to a shorter transition to stage II due to the limitation of capillary flow and the increasing contribution from vapor diffusion inside the porous media.

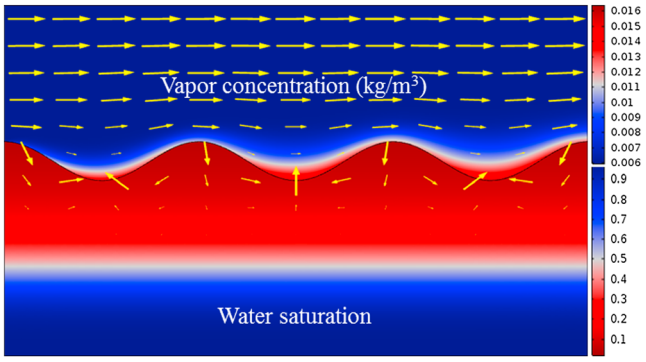

Figure 13. Distribution of vapor concentration (kg/m^3) in the free-flow region and saturation in the porous media (AR = 1/4, the arrows show the gas flows direction and the size of the arrows is proportional to the gas velocity. Separate scales of the arrows are used in free-flow region and porous media).

Similarly, high aspect ratios also result in a large influence of capillary flow. However, the aspect ratio may also influence the vapor diffusion in the boundary layer, which decides the evaporation rate. Figure 13 shows the distribution of vapor concentration in the free-flow region and water saturation in the porous media at t = 40 days. The arrows represent the gas flow direction, and the size of the arrow is proportional to the magnitude of the velocity. Clearly, the vapor accumulates in the valley. Additionally, the near-surface vapor concentration inside the valley increases as the atmospheric air flows from left to the right as shown in Figure 14a. The convex parts correspond to the vapor concentration in the valleys. As what has been mentioned in section 4.1, the distribution of the vapor along the surface is partially due to the surface wind speed distribution. From left to right, the wind slows down when it flows

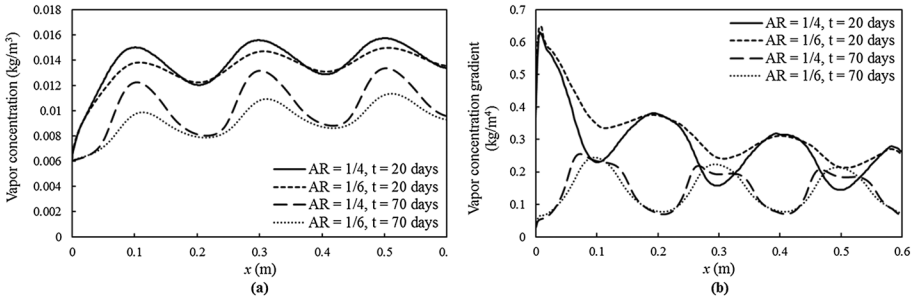

Figure 14. (a) Vapor concentration along soil surface with AR of 1/6 and 1/4 at t = 20 and 70 days. (b) Normal vapor concentration gradient along soil surface with AR of 1/6 and 1/4 at t = 20 and 70 days. AR = aspect ratio.

downward and accelerates when it climbs up. The boundary layer has the largest thickness at the valley within a wavy element. Considering the accumulation of vapor along the surface, the vapor concentration gradient should be smaller at the uphill in a wavy element and becomes increasingly smaller at the later wavy elements (see Figures 13 and 14b). Increasing the aspect ratio will also increase the accumulation of vapor in the valley, resulting in a thicker boundary layer or lower vapor concentration gradient at the soil surface. This is demonstrated by the comparison of the vapor concentration gradient at the soil surface with aspect ratio (AR) of 1/6 and 1/4 at t = 20 days shown in Figure 14b. Therefore, under the reverse effects of capillary flow and vapor diffusion in the boundary layer, the evaporation rate from a large-aspect ratio surface is smaller in stage I, as shown in Figure 12b. If the aspect ratio is infinitely small, the wavy surface reduces to a flat surface. Compared with a wavy surface, the boundary layer of a flat surface is thinner and thus the evaporation rate is larger during stage I as determined by the vapor diffusion in the boundary layer. Likewise, when the influence of capillary flow starts to decline, vapor diffusion in the porous media begins to dominate and the evaporation comes to stage II after a faster decrease during the transition. The higher evaporation rate in stage I leads to faster drop in the transition and lower evaporation rate in stage II. When the vapor diffusion in the porous media becomes a dominant factor during stage II, the vaporization plane has receded downward, which indicates no water can reach the soil surface. Thus, the vapor diffusion across the boundary layer or the vapor concentration gradient at the soil surface will have little influence for different aspect ratios, especially at the surface peaks, due to the higher priority of losing the influence of capillary flow. The comparison of the vapor concentration gradient at the surface with the aspect ratios (AR) of 1/6 and 1/4 at 70 days as shown in Figure 14b indicates this explanation. Figure 12b shows that the 70 days is approximately the end of the transition. We can also see from Figure 14a that at the 70 days, there is still a difference in the vapor concentration between the peaks and valleys of the soil surface. In other words, capillary flow still affects the valleys. This is why the vapor concentration gradients at the valleys are different between the 1/6-AR and 1/4-AR surfaces. Further, one may infer that when the capillary flow loses its influence in the porous media on evaporation, the vapor concentration gradient curve for different aspect ratios becomes constant (approximately a horizontal line). Complementarily speaking, although we could compare the evaporation from wavy and flat soil surface by adjusting AR in the simulation, the comparison is not that meaningful in this study. One of the reasons why we focus on wavy surfaces is that it can be considered as a flat surface with simplified permeable obstacles. The substantial mechanisms controlling wavy- and flat-surface evaporation are the same. The only difference stems from the roughness (namely simplified permeable obstacles), which is discussed in this section in detail.

Figure 14b shows the changes in the vapor concentration gradient along a wavy soil surface with different aspect ratios at 20 and 70 days, demonstrating the nonhorizontal distribution of the evaporative flux along the wavy surface (see Figure 15). For the whole system, since the vapor accumulates in the posterior valleys (see Figures 13 and 14a) resulting in a relatively small vapor concentration gradient, evaporation weakens from inlet to outlet (left to right) and decreases integrally over time. Within one wavy element, the ridge contributes more to the evaporation first when the capillary flow is available at the ridge. It leads to the water lost first at the ridges, which has been shown in Figure 10. Due to less and less continuous water available at the ridges, the vapor concentration gradient decreases, resulting in lower local evaporative flux. As the capillary flow vanishes at the ridge and still exists at the valley, the valley contributes more

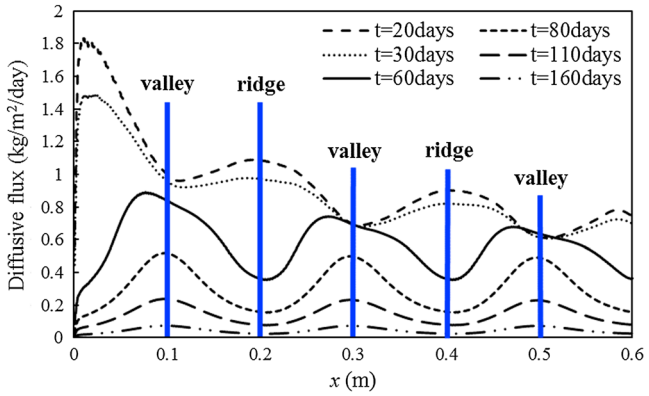

Figure 15. Diffusive flux along soil surface with three waves at t = 20, 30, 60, 80, 110, and 160 days; AR = 1/6.

to evaporation while vapor diffusion dominates at the ridge of the porous media, contributing less although the concentration boundary layer at the valley is thicker than that of the ridge. As capillary flow loses its influence gradually and the evaporation from the whole system is dominated by vapor diffusion in the porous media, the difference of the evaporation between the wavy elements becomes small. The evaporation comes to stage II.

In summary, the influence of the surface structure is relatively complex, since it is related to both the capillary flow and the boundary layer. More waves and steeper waves indicate more influence from capillary flow, enhancing evaporation; while steeper waves also results in a thicker boundary layer and weakens evaporation. Especially, in the case where a generalized top boundary condition consisting of resistance terms is used for the estimation of the evaporation rate from an irregular surface, how to quantify the boundary layer remains an open question.

5. Conclusions

With the goal of coupling free flow and porous media flow to describe evaporation from wavy soil surfaces, we developed a numerical model that describes mass and energy transport processes in and between the subsurface and the atmosphere. The model consists of fluid flow, component and energy equations. What makes this model unique compared with more commonly used evaporation models is that all of the equations are separately defined in both the subsurface and the atmosphere and coupled at the domain interface. To validate the numerical results, we designed a benchmark lab experimental system to simulate evaporation from a wavy soil surface.

At the REV scale, the evaporation stages and the shape of evaporation rate curve is controlled by continuous capillary flow and vapor diffusion within the porous media and across the boundary layer. In theory, the evaporation rate equals the total vapor diffusion in the boundary layer during all evaporation stages. Based on this theory, the influence of atmospheric conditions, soil properties, and macroscale surface roughness on the trend of the evaporation rate curve were discussed. Ambient conditions (e.g., wind speed and temperature) affect the evaporation rate by directly affecting vapor diffusion across the boundary layer. The soil properties directly affect the continuous capillary flow which then influence the vapor concentration gradient in the boundary layer. The macroscale surface roughness directly affects both the capillary flow and vapor diffusion in the boundary layer. The two main parameters that determine the surface structure, surface waves, and aspect ratio, have reverse effects on the evaporation. Increasing the number of surface waves exposes more area (i.e., larger vaporization plane), which allows capillary flow to contribute more during evaporation stage I, resulting in a larger evaporation rate. Although a higher aspect ratio should lead to the same effect, it thickens the boundary layer and changes the vapor diffusion in the boundary layer as well, resulting in a reverse effect compared with the case of more waves. Particularly, the wavy surface reduces to a flat surface when the aspect ratio is infinitely small. Compared with the relatively constant evaporative flux at a flat soil surface, the flux from a wavy surface changes with surface structure, which is also controlled by both capillary flow and the boundary layer.

This study assumes that the air flow in the atmosphere is laminar; however, turbulent flow is more common in nature and easily emerges near wavy surfaces. Therefore, on-going work will incorporate turbulence into the coupled numerical model. Additionally, the laboratory experiment presented herein targets mechanism study and model validation. Considering the application of this experiment in the field or at least within a lysimeter-controlled area, several factors should be taken into account. The first is the definition of a *roughness* size. The influence of aggregate roughness at the soil surface should be distinguished from the macroscale roughness defined in this paper. Second, in field experiments, natural wind speed cannot be controlled. Turbulent and laminar air flow from random directions may appear alternately, and the soil surface may move when exposed to strong wind conditions. Finally, because of the complexity of natural conditions, added factors would need to be incorporated into the model to account for, as an example, solar radiation, precipitation, and runoff. We expect that this study as well as the

planned follow-on work, however, is useful to improving models for evaporation prediction on the engineering scale.

Appendix A

A1. Van Genuchten Model

The van Genuchten model (Van Genuchten, 1980) used in this study to describe the relationship between capillary pressure and water saturation:

$$S_{ew} = \begin{cases} [1 + (\alpha|p_c/\rho_w g|)^n]^{-m} & , \quad p_c > 0 \\ 1 & , \quad p_c \leq 0 \end{cases} \tag{A1}$$

where S_{ew} is the normalized water saturation defined by $S_{ew} = (S_w\text{-}S_{rw})/(1\text{-}S_{wr}\text{-}S_{rg})$, S_{rw} and S_{rg} are residual saturation of water and gas, respectively, and α and n are van Genuchten fitting parameters ($m = 1–1/n$).

The van Genuchten-Mualem model (Van Genuchten, 1980) used to describe the relative permeability of water and gas:

$$\begin{aligned} k_{rw} &= S_{ew}^{l}\left[1 - \left(1 - S_{ew}^{1/m}\right)^{m}\right]^2 \\ k_{rg} &= (1 - S_{ew})^{l}\left(1 - S_{ew}^{1/m}\right)^{2m} \end{aligned} \tag{A2}$$

where l is van Genuchten fitting parameter.

A2. Phase Change Rate

The phase change between the liquid water and water vapor can be defined by a local equilibrium assumption or by considering the nonequilibrium behavior. In hydrologic studies, it is commonly assumed that the water vapor concentration in the air is always in equilibrium with liquid water in the pores. Under this assumption, the phase exchange happens within a negligible time interval. There are also several studies that demonstrated the importance of considering nonequilibrium phase change in modeling efforts of evaporation (Armstrong et al., 1994; Benet & Jouanna, 1982; Smits et al., 2011).

Halder et al. (2011) discussed the equilibrium and nonequilibrium formulation of phase change in detail. Under the equilibrium assumption, the vapor pressure is always equal to the equilibrium vapor pressure at a given temperature and moisture condition. We can calculate the equilibrium vapor pressure based on Kelvin's equation and then the vapor concentration according to Henry's law. Thus, the phase change rate, f_{vw}, comes out of the solution since all the terms on the left-hand side of the component mass balance equation (equation (7)) are known (Halder et al., 2011). In other words, this source term is implicit under the equilibrium assumption, which is difficult to incorporate in the numerical calculation. On the other hand, when we consider nonequilibrium, there is a time interval, Δt, for the system to reach equilibrium after phase change (i.e., evaporation or condensation). A commonly used nonequilibrium phase change rate term is defined by (Bixler, 1985; Smits et al., 2011):

$$f_{vw} = \frac{b\phi(S_w - S_{rw})RT}{M_w}\left(\rho_{v,eq} - \rho_v\right) \tag{A3}$$

where b is a fitting parameter, R is the universal gas constant (8.314 J·mol^{-1}·K^{-1}), M_w is molecular mass (kg/mol), $\rho_{v,eq}$ is the density of vapor at equilibrium (kg/m^3), and ρ_v is the vapor density at any condition (kg/m^3). The vapor density at equilibrium is defined by

$$\rho_{v,eq} = \rho_{v,s}\exp\left(\frac{M_w p_c}{\rho_w RT}\right) \tag{A4}$$

according to Kelvin's equation, where $\rho_{v,s}$ is the saturated vapor density (kg/m^3). The saturated vapor density is estimated empirically (Campbell, 1985):

$$\rho_{v,s} = \frac{\exp\left(31.37 - 6014.79T^{-1} - 7.92\times10^{-3}T\right)}{T}\times10^{-3} \quad \text{(A5)}$$

Clearly, this results in an explicit source term representing liquid-gas phase change rate in the mass balance equation, see equations (5) and (7). According to Halder et al. (2011), the equilibrium time is around 10^{-6} s for a 1-μm distance assuming only pure molecular diffusion exists. In other words, it is meaningless to introduce nonequilibrium phase change if all the transport time scales are much more than the equilibrium time at the same length scale. However, the nonequilibrium phenomenon cannot be ignored if the pore size is equal to or less than 0.1 mm. Therefore, in our simulation where the pore size is approximately 10^{-1} mm, it is necessary to take the nonequilibrium phase change into consideration. The integrated constant coefficient in equation (A3), $B = bRT/M_w$, denotes the reciprocal of the equilibrium time. As the fitting parameter b becomes infinitely large, the nonequilibrium phase change term will reduce to an equilibrium state.

Notation

C_{surf} Surface vapor concentration (kg/m^3).
C_∞ Atmospheric vapor concentration (kg/m^3).
D_v Vapor diffusivity coefficient (m^2/s).
E Evaporation rate (kg/[m·day]).
E_{tot} Cumulative evaporation (kg/m).
K_{int} Intrinsic permeability (m^2).
K_{sat} Saturated hydraulic conductivity (m/s).
L Latent heat of water vaporization (J/kg).
M_w Molecular weight of water (kg/mol).
P A parameter associated with pore radius (m).
Q_s Energy losses from the soil tank (W/m^3).
R Universal gas constant (J/[mol·K]).
R_{BL} Boundary layer resistance (s/m).
R_{sv} Soil resistance (s/m).
S_i Saturation (i = w,g).
S_{ew} Effective water saturation.
T Temperature (K).
U_∞ Atmospheric air flow velocity (m/s).
B Reciprocal of equilibrium time for phase change (1/s).
b Fitting coefficient (s/m^2).
$c_{p,i}$ Heat capacity (i = w,g,s) (J/[kg·K]).
f_{vw} Phase change rate (kg/[m^3·s]).
k_{ri} Relative permeability (i = w,g).
l, m, n Van Genuchten parameter.
p_i Pressure (i = w,g) (Pa).
p_c Capillary pressure (Pa).
p_∞ Atmospheric gas pressure (Pa).
p_s Surface gas pressure (Pa).
r_p Pore radius (m).
t Time (s).
u_i Velocity (i = w,g) (m/s).
w_v Mass fraction of vapor in gas.
n Normal vector.
t Tangential vector.

Greek letter

α Van Genuchten parameter.
α_{BJ} Slip coefficient at the interface.

β	A constant reconciling units.
λ_i	Thermal conductivity (i = w,g,s) (W/[m·K]).
ϕ	Porosity.
τ	Tortuosity.
μ_i	Viscosity (i = w,g) (Pa·s).
δ_{m}	Boundary layer thickness (m).
ρ_i	Density (i = w,g,s) (kg/m^3).
$\rho_{\mathrm{v,s}}$	Saturated vapor density (kg/m^3).
$\rho_{\mathrm{v,eq}}$	Equilibrium vapor density (kg/m^3).
θ_{surf}	Surface water content.
θ_{r}	Residual water content.
Θ_{surf}	Effective surface water content.
υ	A parameter related with flow path geometry and connectivity.

Superscript

ff	Free-flow region.
pm	Porous media.

Subscript

w	Water.
v	Water vapor.
g	Gas.
s	Solid.

Acknowledgments
This research was funded by the National Science Foundation project award 1447533 and the Deutsche Forschungsgemeinschaft (DFG) HE 2531/14-1. The authors would like to thank the valuable discussions with Thomas Fetzer from the University of Stuttgart, Erfan Haghighi from Massachusetts Institute of Technology, and the experimental assistance from Zhen Li from Colorado School of Mines. The original experimental data used in this study are presented in the supporting information.

References

Armstrong, J. E., Frind, E. O., & McClellan, R. D. (1994). Nonequilibrium mass transfer between the vapor, aqueous, and solid phases in unsaturated soils during vapor extraction. *Water Resources Research*, *30*(2), 355–368. https://doi.org/10.1029/93WR02481

Assouline, S. (2006). Modeling the relationship between soil bulk density and the water retention curve. *Vadose Zone Journal*, *5*(2), 554–563. https://doi.org/10.2136/vzj2005.0083

Baber, K. (2014). *Coupling free flow and flow in porous media in biological and technical applications: From a simple to a complex interface description*.

Baber, K., Mosthaf, K., Flemisch, B., Helmig, R., Müthing, S., & Wohlmuth, B. (2012). Numerical scheme for coupling two-phase compositional porous-media flow and one-phase compositional free flow. *The IMA Journal of Applied Mathematics*, *77*(6), 887–909. https://doi.org/10.1093/imamat/hxs048

Baskaran, V., Smits, A. J., & Joubert, P. N. (1987). A turbulent flow over a curved hill: Part 1. Growth of an internal boundary layer. *Journal of Fluid Mechanics*, *182*, 47–83. https://doi.org/10.1017/S0022112087002246

Bear, J. (2013). *Dynamics of fluids in porous media*. Courier Corporation.

Beavers, G. S., & Joseph, D. D. (1967). Boundary conditions at a naturally permeable wall. *Journal of Fluid Mechanics*, *30*(01), 197–207. https://doi.org/10.1017/S0022112067001375

Benet, J. C., & Jouanna, P. (1982). Phenomenological relation of phase change of water in a porous medium: Experimental verification and measurement of the phenomenological coefficient. *International Journal of Heat and Mass Transfer*, *25*(11), 1747–1754. https://doi.org/10.1016/0017-9310(82)90154-5

Bird, R. B., Stewart, W. E., & Lightfoot, E. N. (2004). *Transport phenomena. 2002*. New York: John Wiley.

Bixler, N. E. (1985). *NORIA: A finite element computer program for analyzing water, vapor, air and energy transport in porous media*. Albuquerque, NM: Sandia National Laboratories.

Brutsaert, W. (1982). *Evaporation into the Atmosphere. Theory, History, and Applications*. Dordrecht: Holland, D. Reidel Co.

Buckles, J., Hanratty, T. J., & Adrian, R. J. (1984). Turbulent flow over large-amplitude wavy surfaces. *Journal of Fluid Mechanics*, *140*, 27–44. https://doi.org/10.1017/S0022112084000495

Budagovskij, A. I. (1964). *Evaporation of soil water*. Moscow: Izdatelsrvo Nauka (Publishers Nauka).

Campbell, G. S. (1985). *Soil physics with BASIC: Transport models for soil-plant systems*. Amsterdam: Elsevier.

Canovaro, F., Paris, E., & Solari, L. (2007). Effects of macro-scale bed roughness geometry on flow resistance. *Water Resources Research*, *43*, W10414. https://doi.org/10.1029/2006WR005727

Chamindu Deepagoda, T. K. K., Smits, K., Ramirez, J., & Moldrup, P. (2016). Characterization of thermal, hydraulic, and gas diffusion properties in variably saturated sand grades. *Vadose Zone Journal*, *15*(4). https://doi.org/10.2136/vzj2015.07.0097

Cherukat, P., Na, Y., Hanratty, T. J., & McLaughlin, J. B. (1998). Direct numerical simulation of a fully developed turbulent flow over a wavy wall. *Theoretical and Computational Fluid Dynamics*, *11*(2), 109–134. https://doi.org/10.1007/s001620050083

Comsol (2016). COMSOL multiphysics: Version 5.2a. Comsol

Davarzani, H., Smits, K., Tolene, R. M., & Illangasekare, T. (2014). Study of the effect of wind speed on evaporation from soil through integrated modeling of the atmospheric boundary layer and shallow subsurface. *Water Resources Research*, *50*, 661–680. https://doi.org/10.1002/2013WR013952

Fetzer, T. (2012). Numerical analysis of the influence of turbulence on exchange processes between porous-medium and free flow. *Dep. of Hydromech. and Model. of Hydrosyst., IWS, Univ. of Stuttgart, Stuttgart, Germany*.

Fetzer, T., Smits, K. M., & Helmig, R. (2016). Effect of turbulence and roughness on coupled porous-medium/free-flow exchange processes. *Transport in Porous Media*, *114*(2), 395–424. https://doi.org/10.1007/s11242-016-0654-6

Forsythe, L. F. (2017). A numerical and experimental analysis of bare soil resistance in homogeneous and heterogeneous soils (Doctoral dissertation, Colorado School of Mines. Arthur Lakes Library).

Goyeau, B., Lhuillier, D., Gobin, D., & Velarde, M. G. (2003). Momentum transport at a fluid–porous interface. *International Journal of Heat and Mass Transfer*, *46*(21), 4071–4081. https://doi.org/10.1016/S0017-9310(03)00241-2

Guzha, A. C. (2004). Effects of tillage on soil microrelief, surface depression storage and soil water storage. *Soil and Tillage Research*, *76*(2), 105–114. https://doi.org/10.1016/j.still.2003.09.002

Haghighi, E., & Or, D. (2015). Evaporation from wavy porous surfaces into turbulent airflows. *Transport in Porous Media*, *110*(2), 225–250. https://doi.org/10.1007/s11242-015-0512-y

Haghighi, E., Shahraeeni, E., Lehmann, P., & Or, D. (2013). Evaporation rates across a convective air boundary layer are dominated by diffusion. *Water Resources Research*, *49*, 1602–1610. https://doi.org/10.1002/wrcr.20166

Halder, A., Dhall, A., & Datta, A. K. (2011). Modeling transport in porous media with phase change: Applications to food processing. *Journal of Heat Transfer*, *133*(3), 031010. https://doi.org/10.1115/1.4002463

Han, D., Sun, D., & Wang, X. (2014). Two-phase flows in karstic geometry. *Mathematical Methods in the Applied Sciences*, *37*(18), 3048–3063. https://doi.org/10.1002/mma.3043

Huang, Z. Q., Gao, B., Zhang, X. Y., & Yao, J. (2016). On the coupling of two-phase free flow and porous flow. In *ECMOR XV-15th European Conference on the Mathematics of Oil Recovery*.

Huxman, T. E., Wilcox, B. P., Breshears, D. D., Scott, R. L., Snyder, K. A., Small, E. E., Hultine, K., et al. (2005). Ecohydrological implications of woody plant encroachment. *Ecology*, *86*(2), 308–319. https://doi.org/10.1890/03-0583

Kaviany, M. (2002). *Principles of heat transfer*. New York: John Wiley.

Kool, D., Agam, N., Lazarovitch, N., Heitman, J. L., Sauer, T. J., & Ben-Gal, A. (2014). A review of approaches for evapotranspiration partitioning. *Agricultural and Forest Meteorology*, *184*, 56–70. https://doi.org/10.1016/j.agrformet.2013.09.003

Kruse, N., Kuhn, S., & von Rohr, P. R. (2006). Wavy wall effects on turbulence production and large-scale modes. *Journal of Turbulence*, *7*, N31. https://doi.org/10.1080/14685240600602911

Kustas, W. P., & Agam, N. (2014). Soil evaporation. *Encyclopedia of Natural Resources*. https://doi.org/10.1081/E-ENRL-120049129

Lehmann, P., Assouline, S., & Or, D. (2008). Characteristic lengths affecting evaporative drying of porous media. *Physical Review E*, *77*(5), 056309.

Lehrsch, G. A., Whisler, F. D., & Römkens, M. J. M. (1987). Soil surface roughness as influenced by selected soil physical properties. *Soil and Tillage Research*, *10*(3), 197–212. https://doi.org/10.1016/0167-1987(87)90028-6

Maaß, C., & Schumann, U. (1996). Direct numerical simulation of separated turbulent flow over a wavy boundary. In *Flow Simulation with high-performance computers II* (pp. 227–241). Wiesbaden, Germany: Vieweg + Teubner Verlag.

Matthias, A. D., Fimbres, A., Sano, E. E., Post, D. F., Accioly, L., Batchily, A. K., & Ferreira, L. G. (2000). Surface roughness effects on soil albedo. *Soil Science Society of America Journal*, *64*(3), 1035–1041. https://doi.org/10.2136/sssaj2000.6431035x

Merta, M., Seidler, C., & Fjodorowa, T. (2006). Estimation of evaporation components in agricultural crops. *Biologia*, *61*(19), S280–S283.

Millington, R. J., & Quirk, J. P. (1961). Permeability of porous solids. *Transactions of the Faraday Society*, *57*, 1200–1207. https://doi.org/10.1039/tf9615701200

Moradi, A., Smits, K. M., Massey, J., Cihan, A., & McCartney, J. (2015). Impact of coupled heat transfer and water flow on soil borehole thermal energy storage (SBTES) systems: Experimental and modeling investigation. *Geothermics*, *57*, 56–72. https://doi.org/10.1016/j.geothermics.2015.05.007

Morton, F. I. (1983). Operational estimates of areal evapotranspiration and their significance to the science and practice of hydrology. *Journal of Hydrology*, *66*(1–4), 1–76. https://doi.org/10.1016/0022-1694(83)90177-4

Mosthaf, K. (2014). Modeling and analysis of coupled porous-medium and free flow with application to evaporation processes.

Mosthaf, K., Baber, K., Flemisch, B., Helmig, R., Leijnse, A., Rybak, I., & Wohlmuth, B. (2011). A coupling concept for two-phase compositional porous-medium and single-phase compositional free flow. *Water Resources Research*, *47*, W10522. https://doi.org/10.1029/2011WR010685

Mosthaf, K., Helmig, R., & Or, D. (2014). Modeling and analysis of evaporation processes from porous media on the REV scale. *Water Resources Research*, *50*, 1059–1079. https://doi.org/10.1002/2013WR014442

Mwendera, E. J., & Feyen, J. (1997). Tillage and evaporativity effects on the drying characteristics of a silty loam: Evaporation prediction models. *Soil and Tillage Research*, *41*(1–2), 127–140. https://doi.org/10.1016/S0167-1987(96)01078-1

Nield, D. A., Bejan, A., & Nield-Bejan, D. (2006). *Convection in porous media* (Vol. 3). New York: Springer.

Oleson, K. W., Lawrence, D. M., Gordon, B., Flanner, M. G., Kluzek, E., Peter, J., et al. (2010). Technical description of version 4.0 of the community land model (CLM).

Perry, A. E., Schofield, W. H., & Joubert, P. N. (1969). Rough wall turbulent boundary layers. *Journal of Fluid Mechanics*, *37*(02), 383–413. https://doi.org/10.1017/S0022112069000619

Potter, K. N., Horton, R., & Cruse, R. M. (1987). Soil surface roughness effects on radiation reflectance and soil heat flux. *Soil Science Society of America Journal*, *51*(4), 855–860. https://doi.org/10.2136/sssaj1987.03615995005100040003x

Pourbakhtiar, A., Poulsen, T. G., Wilkinson, S., & Bridge, J. W. (2017). Effect of wind turbulence on gas transport in porous media: Experimental method and preliminary results. *European Journal of Soil Science*, *68*(1), 48–56. https://doi.org/10.1111/ejss.12403

Raupach, M. R., & Finnigan, J. J. (1997). The influence of topography on meteorogical variables and surface-atmosphere interactions. *Journal of Hydrology*, *190*(3–4), 182–213. https://doi.org/10.1016/S0022-1694(96)03127-7

Sakai, M., Jones, S. B., & Tuller, M. (2011). Numerical evaluation of subsurface soil water evaporation derived from sensible heat balance. *Water Resources Research*, *47*, W02547. https://doi.org/10.1029/2010WR009866

Sakaki, T., & Illangasekare, T. H. (2007). Comparison of height-averaged and point-measured capillary pressure–saturation relations for sands using a modified Tempe cell. *Water Resources Research*, *43*, W12502. https://doi.org/10.1029/2006WR005814

Sakaki, T., Limsuwat, A., Smits, K. M., & Illangasekare, T. H. (2008). Empirical two-point α-mixing model for calibrating the ECH2O EC-5 soil moisture sensor in sands. *Water Resources Research*, *44*, W00D08. https://doi.org/10.1029/2008WR006870

Shahraeeni, E., Lehmann, P., & Or, D. (2012). Coupling of evaporative fluxes from drying porous surfaces with air boundary layer: Characteristics of evaporation from discrete pores. *Water Resources Research*, *48*, W09525. https://doi.org/10.1029/2012WR011857

Shao, W., Coenders-Gerrits, M., Judge, J., Zeng, Y., & Su, Y. (2018). The impact of non-isothermal soil moisture transport on evaporation fluxes in a maize cropland. *Journal of Hydrology*, *561*, 833–847. https://doi.org/10.1016/j.jhydrol.2018.04.033

Shuttleworth, W. J. (2007). Putting the "vap" into evaporation. *Hydrology and Earth System Sciences Discussions*, *11*(1), 210–244. https://doi.org/10.5194/hess-11-210-2007

Smits, K. M., Cihan, A., Sakaki, T., & Illangasekare, T. H. (2011). Evaporation from soils under thermal boundary conditions: Experimental and modeling investigation to compare equilibrium-and nonequilibrium-based approaches. *Water Resources Research*, *47*, W05540. https://doi.org/10.1029/2010WR009533

Swenson, S. C., & Lawrence, D. M. (2014). Assessing a dry surface layer-based soil resistance parameterization for the community land model using GRACE and FLUXNET-MTE data. *Journal of Geophysical Research: Atmospheres*, *119*, 10,299–10,312. https://doi.org/10.1002/2014JD022314

Tang, J. Y., & Riley, W. J. (2013). A new top boundary condition for modeling surface diffusive exchange of a generic volatile tracer: Theoretical analysis and application to soil evaporation. *Hydrology and Earth System Sciences*, *17*(2), 873–893. https://doi.org/10.5194/hess-17-873-2013

Taylor, P. A., & Gent, P. R. (1974). A model of atmospheric boundary-layer flow above an isolated two-dimensional 'hill'; an example of flow above "gentle topography". *Boundary-Layer Meteorology*, *7*(3), 349–362. https://doi.org/10.1007/BF00240837

Tezduyar, T. E., Sathe, S., Schwaab, M., & Conklin, B. S. (2008). Arterial fluid mechanics modeling with the stabilized space–time fluid–structure interaction technique. *International Journal for Numerical Methods in Fluids*, *57*(5), 601–629. https://doi.org/10.1002/fld.1633

Unger, P. W., & Cassel, D. (1991). Tillage implement disturbance effects on soil properties related to soil and water conservation: A literature review. *Soil and Tillage Research*, *19*(4), 363–382. https://doi.org/10.1016/0167-1987(91)90113-C

Van Genuchten, M. T. (1980). A closed-form equation for predicting the hydraulic conductivity of unsaturated soils. *Soil Science Society of America Journal*, *44*(5), 892–898. https://doi.org/10.2136/sssaj1980.03615995004400050002x

Vanderborght, J., Fetzer, T., Mosthaf, K., Smits, K. M., & Helmig, R. (2017). Heat and water transport in soils and across the soil-atmosphere interface: 1. Theory and different model concepts. *Water Resources Research*, *53*, 1057–1079. https://doi.org/10.1002/2016WR019982

Wagner, C., Kenjereš, S., & von Rohr, P. R. (2011). Dynamic large eddy simulations of momentum and wall heat transfer in forced convection over wavy surfaces. *Journal of Turbulence*, *12*, N7. https://doi.org/10.1080/14685248.2010.547496

Weaver, J. W., & Tillman, F. D. (2005). *Uncertainty and the Johnson-Ettinger model for vapor intrusion calculations*. Washington, DC: US Environmental Protection Agency, Office of Research and Development.

Whitaker, S. (1977). Simultaneous heat, mass, and momentum transfer in porous media: A theory of drying. *Advances in Heat Transfer*, *13*, 119–203. https://doi.org/10.1016/S0065-2717(08)70223-5

Zhang, C., Werth, C. J., & Webb, A. G. (2008). Investigation of surfactant-enhanced mass removal and flux reduction in 3D correlated permeability fields using magnetic resonance imaging. *Journal of Contaminant Hydrology*, *100*(3-4), 116–126. https://doi.org/10.1016/j.jconhyd.2008.06.002

Zilker, D. P., & Hanratty, T. J. (1979). Influence of the amplitude of a solid wavy wall on a turbulent flow. Part 2. Separated flows. *Journal of Fluid Mechanics*, *90*(02), 257–271. https://doi.org/10.1017/S0022112079002196